SCIENCE CHINA
Technological Sciences

• Article •

doi: 10.1007/s11431-015-5907-z

Two-dimensional numerical manifold method with multilayer covers

LIU ZhiJun[1] & ZHENG Hong[2*]

[1] *State Key Laboratory of Geomechanics and Geotechnical Engineering, Institute of Rock and Soil Mechanics, Chinese Academy of Sciences, Wuhan 430071, China;*

[2] *Key Laboratory of Urban Security and Disaster Engineering, Ministry of Education, Beijing University of Technology, Beijing 100124, China*

Received April 15, 2015; accepted July 27, 2015

In order to reach the best numerical properties with the numerical manifold method (NMM), uniform finite element meshes are always favorite while constructing mathematical covers, where all the elements are congruent. In the presence of steep gradients or strong singularities, in principle, the locally-defined special functions can be added into the NMM space by means of the partition of unity, but they are not available to those complex problems with heterogeneity or nonlinearity, necessitating local refinement on uniform meshes. This is believed to be one of the most important open issues in NMM. In this study multilayer covers are proposed to solve this issue. In addition to the first layer cover which is the global cover and covers the whole problem domain, the second and higher layer covers with smaller elements, called local covers, are used to cover those local regions with steep gradients or strong singularities. The global cover and the local covers have their own partition of unity, and they all participate in the approximation to the solution. Being advantageous over the existing procedures, the proposed approach is easy to deal with any arbitrary-layer hanging nodes with no need to construct super-elements with variable number of edge nodes or introduce the Lagrange multipliers to enforce the continuity between small and big elements. With no limitation to cover layers, meanwhile, the creation of an even error distribution over the whole problem domain is significantly facilitated. Some typical examples with steep gradients or strong singularities are analyzed to demonstrate the capacity of the proposed approach.

numerical manifold method, finite element method, covers, hanging nodes, structured local refinement, short cracks

Citation: Liu Z J, Zheng H. Two-dimensional numerical manifold method with multilayer covers. Sci China Tech Sci, doi: 10.1007/s11431-015-5907-z

1 Introduction

In order to solve in a unified way geotechnical problems from continua to discontinua, Shi laid out the framework of the numerical manifold method (NMM) [1] in 1991 after he developed the discontinuous deformation analysis (DDA) in 1985. Since then, great progress has been made in both theories and applications of NMM.

Lin [2] discussed the relationship between NMM and other numerical methods that were also based on the partition of unity notion [3] but invented later such as the generalized finite element method (GFEM) [4], the extended finite element method (XFEM) [5], and the element-free Galerkin method (EFG) [6].

Terada et al. [7] gave NMM an alias, the finite cover method (FCM), and successfully applied FCM to the analysis of inclusion problems.

One important attribute of NMM is that it is able to en-

*Corresponding author (email: hzheng@whrsm.ac.cn)

hance the degree of interpolation polynomials without adding new nodes, see the works by Chen et al. [8] and Jiang et al. [9], which, however, incurs the same linear dependency issue as in GFEM. Tian et al. [10] gave a thorough review on this issue and proposed that the distorted quadrilateral elements be deployed along the essential boundary to overcome the linear dependency. With the topological information inherent in the finite element mesh, An et al. [11] developed an algorithm for predicting the rank deficiency of the stiffness matrix. Recently, they proved the linear independency of the flat-top PU-based high-order polynomial approximation [12]. Cai et al. [13] suggested a configuration of degrees of freedom free from the rank dependency issue, where incomplete quadratic polynomials excluding monomials of x^2 and y^2 were assigned to the stars of inner nodes, while constants to the patches of nodes on the displacement boundary.

NMM possesses excellent numerical properties. For example, Terada and Kurumatani [14] tested a number of elasticity problems by FCM and FEM respectively, and concluded that the performance deterioration due to element distortion is less serious than that in FEM. Even for those problems with strong singularities, furthermore, NMM has been shown by Zheng and Xu [15] to be mesh independent.

The major purpose for Shi to invent NMM is to solve in a unified way the problems involving continuous and discontinuous deformations. Wu and Wong [16], Kurumatani and Terada [17], Ma et al. [18], and many others, have made great efforts to investigate the crack analysis and propagation of cracks in geomaterials. An et al. [19] made a comparison between NMM and the extended finite element method (XFEM) in simulating discontinuities. Ning et al. [20] carried out an analysis of slope dynamic failure involving crack growth. Wu and Wong [21] simulated initiation and propagation of frictional cracks which arise from geomechanics. Recently, Zheng and Xu [15] proposed a simpler and more efficient scheme for the integration of $1/r$ singularity due to crack tips, and gave a proper representation of the displacement field around a kinked crack tip. Of course, there are some other methods, such as [22], which are designed ad hoc to simulate cracking of rocks.

In addition to the application to solids, Zhang et al. [23] solved Navier–Stokes equations for fluid flow, where the same mesh was used to approximate both velocity and pressure. It is believed that NMM will have more extensive applications in the simulation of seepage flow through fractal fracture networks [24].

All the above investigations and developments of NMM are limited to the second order partial differential equations where the NMM space takes on the Lagrange form. For the fourth order partial differential equations, Zheng et al. [25] proposed the NMM space of Hermit form and applied it to Kirchhoff's thin plate problems.

Although the mathematical covers of NMM can be constructed with a series of simple domains of any shape, for example, the influential domains of scattered nodes in the moving least squares (MLS) as in refs. [26–28] or honeycomb meshes as in ref. [29], so far in almost all the applications and developments of NMM finite element meshes have been chosen as the mathematical covers. This is because the finite element methods are most familiar to engineers and affluent knowledge and experience have been accumulated. In this case, the inventor of NMM always advocates uniform meshes as mathematical covers, where all the elements are congruent, so that the highest interpolation accuracy is reached [30]. Where singularities or steep gradients are present, in principle we can enrich the NMM space with those locally defined functions that well reflect the behaviors of solution over the local regions. However, only limited *a priori* knowledge about the solution is available for many problems of engineering relevance, especially for nonlinear problems. Control of discretization errors in this class of problems requires local mesh refinement which offsets some of the advantages associated with local enrichment techniques.

If an unstructured mesh is used for local refinement, where some distorted elements exist, NMM will lose its excellent numerical properties and reduces to the conventional finite element method. Sticking to uniform meshes, the structured local refinement must create irregular meshes as illustrated in Figure 1, where hanging nodes, marked by "○", are present. Since NMM was invented, the inventor and many others have been considering how to realize the structured local refinement in the framework of NMM. This is believed to be one of the most important open issues in NMM. This study aims to solve this issue and is organized as follows.

Considering that NMM is not familiar to many researchers, in Section 2 we concisely reformulate NMM in the framework of general covers. Section 3 recapitulates NMM in the setting of finite element covers. In Section 4, firstly we make a review on the structured local refinement, where we see that the existing treatments of hanging nodes are

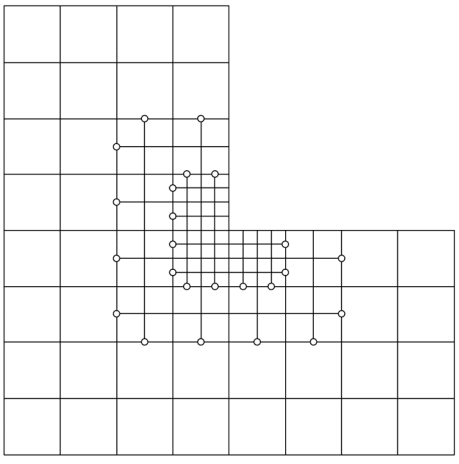

Figure 1 Irregular mesh caused by local refinement with structured mesh. Nodes marked by ○ are hanging nodes.

hard to be amenable to NMM; then we turn to the topic of this study and, by resorting to the approach of s-FEM [31], we expound NMM with multilayer covers. By the proposed procedure, we do not need to construct *ad hoc* new super-elements that are appropriate for irregular meshes with no variational crime, nor yet to introduce the Lagrange multipliers to enforce the continuity between small and big elements. In Section 5, we use some typical examples with steep gradients or strong singularities to demonstrate the capacity of the proposed procedure, and make comparisons with the existing treatments of hanging nodes. Section 6 concludes this study with some discussions.

2 Review on the conventional NMM

NMM, to our knowledge, consists of four parts, the cover systems, the partition of unity, the NMM space, and the variational principle fitted to NMM.

2.1 The general cover systems

To solve continuous and discontinuous problems in a unified way, two covers are introduced in NMM, the mathematical cover (MC) and the physical cover (PC).

Throughout this study, Ω represents a 2-dimensional domain of interest. MC consists of m simply connected domains, denoted by M_i, i=1,⋯, m. Each M_i is called a mathematical patch. While deploying MC, we do not have to pay too much concern to the details of Ω. In principle, the only indispensable requirement is that the union of all M_i cover Ω, i.e.,

$$\Omega \subset \bigcup_{i=1}^{m} M_i. \tag{1}$$

The MC configuration is a key factor to the solution precision.

Now we use the components of Ω, including the domain's boundary, the material interface, and the crack, to cut all M_i. Discarding those outside Ω, we obtain p separated domains, P_j, j=1,⋯, p. Each P_j is called a physical patch, which may contain a crack tip or a concave angle. The collection of all the p physical patches constitutes PC, and the union of them covers Ω exactly, i.e.,

$$\Omega = \bigcup_{i=1}^{p} P_i. \tag{2}$$

The overlapping domains of as many as possible physical patches are called manifold elements, which can serve as basic units for integrating the weak form of the problem.

Now we use an example to interpret the conceptions of MC, PC and manifold elements.

Figure 2 illustrates a planar domain Ω containing a branched crack. Let's use three mathematical patches in Figure 3, M_1, M_2 and M_3, to cover Ω. Figure 4 displays all the resulting five physical patches after using the components of Ω to cut M_1, M_2 and M_3. P_1 containing crack tips A and C (Figure 4(a)) is generated from M_1; from M_2 are two separate physical patches P_2 and P_3 (Figure 4(b)), with P_3 containing crack tip B; and from M_3 are two separate physical patches P_4 and P_5 (Figure 4(c)), with P_4 containing crack tip A. All the physical patches, P_1 to P_5, constitute the PC of Ω.

By overlapping the physical patches, P_1 to P_5, we obtain eleven manifold elements, E_1 to E_{11}, as shown in Figure 5. Table 1 lists the eleven manifold elements and the physical patches containing each of the manifold elements. Since only three mathematical patches are used, the number of physical patches containing a manifold element is at most three.

2.2 The partition of unity

(1) Once we have the MC $\{M_i\}_1^m$, we can construct weight functions $w_i(\boldsymbol{r})$, i = 1,⋯, m, with $\boldsymbol{r}$ the position vector, satisfying the following properties:

$$w_i(\boldsymbol{r}) = 0, \text{ if } \boldsymbol{r} \notin M_i, \tag{3.1}$$

$$0 \leqslant w_i(\boldsymbol{r}) \leqslant 1, \text{ if } \boldsymbol{r} \in M_i, \tag{3.2}$$

$$\sum_{i=1}^{m} w_i(\boldsymbol{r}) = 1, \text{ if } \boldsymbol{r} \in \Omega, \tag{3.3}$$

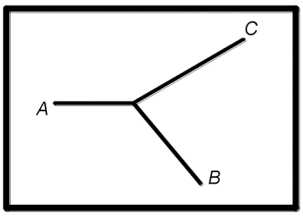

Figure 2 Problem domain containing a bifurcation crack.

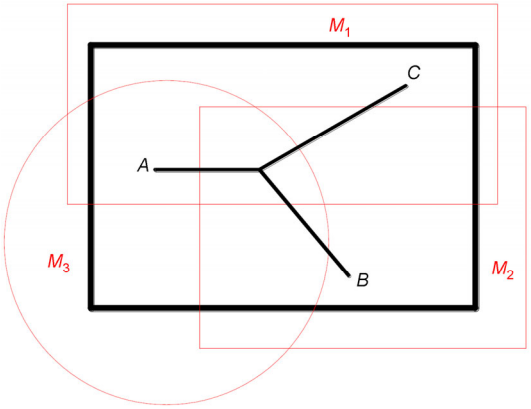

Figure 3 (Color online) Mathematical cover.

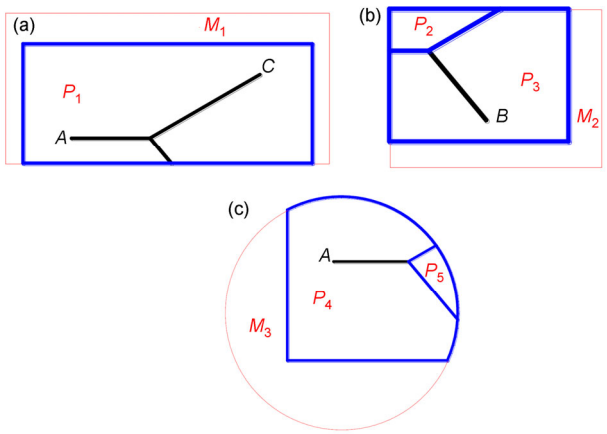

Figure 4 (Color online) Mathematical patches and the resulting physical patches. (a) Physical patch P_1 from M_1; (b) physical patches P_2 and P_3 from M_2; (c) physical patches P_4 and P_5 from M_3.

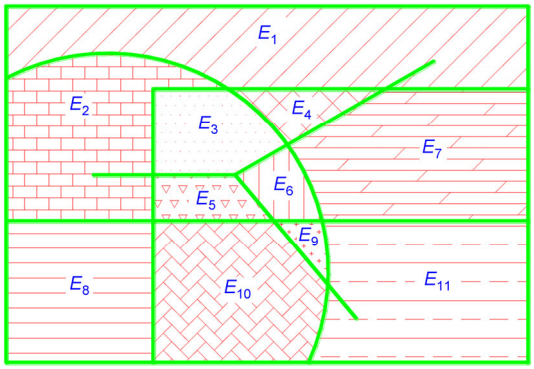

Figure 5 (Color online) Eleven manifold elements.

Table 1 Relation between manifold elements and physical patches

Elem	Covered by physical patches
E_1	P_1
E_2	P_1, P_4
E_3	P_1, P_2, P_4
E_4	P_1, P_2
E_5	P_1, P_3, P_4
E_6	P_1, P_3, P_5
E_7	P_1, P_3
E_8	P_4
E_9	P_3, P_5
E_{10}	P_3, P_4
E_{11}	P_3

$\{w_i(\boldsymbol{r})\}$ is collectively called the partition of unity subordinate to $\{M_i\}$.

In the partition of unity method (PUM) [3], the requirement for $w_i(\boldsymbol{r})\geqslant 0$ is discarded, which is different a little from the standard statements of the partition of unity theorem [32]. The purpose for this, in our opinion, is to include the experiences gained in the finite element analysis, where the shape functions of a nonlinear isoparametric element, such as the 2-dimensional isoparametric element of eight nodes, are negative in part of the element.

Meanwhile, all $w_i(\boldsymbol{r})$ can be made arbitrarily smooth over the whole domain according to the partition of unity theorem [32]. In our cases, nevertheless, we only require $w_i(\boldsymbol{r})$ is continuous, implying that $w_i(\boldsymbol{r})$ vanishes on the boundary of M_i.

(2) By restricting each $w_i(\boldsymbol{r})$ supported by M_i onto the physical patches P_j, generated from M_i, we obtain the partition of unity subordinate to the PC $\{P_j\}_1^p$, still represented by $w_j(\boldsymbol{r})$, $j = 1,\cdots, p$. We further notice that $w_j(\boldsymbol{r})$ on P_j may not be zero on the portion of the boundary of P_j that belongs to a discontinuity (weak or strong).

2.3 The NMM space

Compared with FEM, NMM pays more attention to physical patches rather than individual elements. Over each physical patch, P_j, we independently construct approximations to the solution such that they reflect the local behavior of the solution over P_j.

2.3.1 Approximations over individual physical patches

The approximations over a typical physical patch, P_j, are usually constructed by the Taylor expansion of solution $\boldsymbol{u}$ with regard to a reference point $\boldsymbol{r}_j$,

$$\boldsymbol{u}_j^h(\boldsymbol{r}) = \boldsymbol{u}_j + \sum_{i=1}\frac{1}{i!}\left[(\boldsymbol{r}-\boldsymbol{r}_j)\cdot\frac{\partial}{\partial \boldsymbol{r}}\right]^i \boldsymbol{u}(\boldsymbol{r}_j),\ \forall \boldsymbol{r}\in P_j, \tag{4}$$

with $\boldsymbol{u}_j$=$\boldsymbol{u}(\boldsymbol{r}_j)$, if patch P_j contains no singularity, which is called a nonsingular patch.

To avoid unnecessary distractions, this study takes constants over nonsingular patches, resulting in

$$\boldsymbol{u}_j^h(\boldsymbol{r}) = \boldsymbol{u}_j,\quad \forall \boldsymbol{r}\in P_j. \tag{5}$$

As for the higher order approximations, we refer to refs. [8,15].

If, however, patch P_j contains a crack tip such as P_3 in Figure 4(b), we can enrich the approximations over P_j by adding some particular functions that can reflect the local behavior of the solution over P_j, such as,

$$\boldsymbol{u}_j^h(\boldsymbol{r}) = \boldsymbol{u}_j + \boldsymbol{f}_j(r,\theta), \tag{6}$$

with

$$\boldsymbol{f}_j(r,\theta) = \boldsymbol{E}_j(r,\theta)\boldsymbol{e}_j, \tag{7}$$

$\boldsymbol{e}_j$ is the 8-dimensioanl vector consisting of eight enrichment degrees of freedom

$$\boldsymbol{e}_j^{\mathrm{T}} = \left(e_j^1,\ \cdots,\ e_j^8\right). \tag{8}$$

$\boldsymbol{E}_j(r,\theta)$ is the 2×8 matrix with four enrichment functions

$$\boldsymbol{E}_j = \left[c_1\boldsymbol{I}_2\quad s_1\boldsymbol{I}_2\quad c_2\boldsymbol{I}_2\quad s_2\boldsymbol{I}_2\right], \tag{9}$$

where $\boldsymbol{I}_2$ is the 2 by 2 identity matrix, (c_1, s_1) and (c_2, s_2) are the first two items of Williams' displacement series, defined by

$$\begin{aligned} c_k(r,\theta) &= \sqrt{r}\cos\frac{2k-1}{2}\theta, \\ s_k(r,\theta) &= \sqrt{r}\sin\frac{2k-1}{2}\theta, \end{aligned} \tag{10}$$

with k=1 and 2. Here, (r, θ) is the polar coordinate with the origin at the crack tip, the crack as the polar axis, and $-\pi<\theta\leqslant\pi$.

If more than one crack tip terminates inside P_j, in principle we can enrich the local approximations over P_j by adding more items, like $\boldsymbol{E}_j^2\boldsymbol{e}_j^2$, $\boldsymbol{E}_j^3\boldsymbol{e}_j^3, \cdots$, corresponding to the second tip, the third tip,···, respectively. Therefore, NMM can simulate multiple cracks very naturally.

Eqs. (5) and (6) can be written in the unified form

$$\boldsymbol{u}_j^h(\boldsymbol{r}) = \boldsymbol{L}_j(\boldsymbol{r})\boldsymbol{d}_j, \tag{11}$$

with the vector

$$\boldsymbol{d}_j = \boldsymbol{u}_j, \quad \text{for } P_j \text{ nonsingular}, \tag{12.1}$$

or

$$\boldsymbol{d}_j = \begin{pmatrix} \boldsymbol{u}_j \\ \boldsymbol{e}_j \end{pmatrix}, \quad \text{for } P_j \text{ singular}; \tag{12.2}$$

and the matrix

$$\boldsymbol{L}_j = \boldsymbol{I}_2, \quad \text{for } P_j \text{ nonsingular}, \tag{13.1}$$

or

$$\boldsymbol{L}_j = \begin{bmatrix} \boldsymbol{I}_2 & \boldsymbol{E}_j \end{bmatrix}, \quad \text{for } P_j \text{ singular}, \tag{13.2}$$

which is continuous in P_j.

2.3.2 Global approximations over the problem domain

By adding up the weighted approximations, $w_j\boldsymbol{u}_j^h$, over all the p physical patches, we obtain the global approximation over Ω

$$\boldsymbol{u}^h(\boldsymbol{r}) = \sum_{j=1}^{p} w_j(\boldsymbol{r})\boldsymbol{u}_j^h(\boldsymbol{r}), \quad \forall \boldsymbol{r} \in \Omega. \tag{14}$$

Substituting eq. (11) into eq. (14) results in

$$\boldsymbol{u}^h(\boldsymbol{r}) = \boldsymbol{N}\boldsymbol{d}, \tag{15}$$

where $\boldsymbol{d}$ is the vector consisting of degrees of freedom of all physical patches, and $\boldsymbol{N}$ is the shape matrix defined by

$$\boldsymbol{N} = \begin{bmatrix} w_1\boldsymbol{L}_1, & \cdots, & w_p\boldsymbol{L}_p \end{bmatrix}, \tag{16}$$

which is discontinuous across any discontinuity, weak or strong.

We note in passing that eq. (14) is the Lagrange form of the NMM space, which is appropriate for the second order partial differential equation problems. If a fourth order problem is solved, we should apply the Hermit form of the NMM space, as in ref. [25].

2.3.3 Variational principle fitted to NMM

The conventional minimum potential principle of elasticity says that the real displacement vector $\boldsymbol{u}$ minimizes the potential

$$\pi_c(\mathbf{v}) = \frac{1}{2}\int_{\Omega} \boldsymbol{\varepsilon}^{\mathrm{T}}\boldsymbol{\sigma}\mathrm{d}\Omega - \int_{S^\sigma} \boldsymbol{v}^{\mathrm{T}}\bar{\boldsymbol{p}}\mathrm{d}S, \tag{17}$$

where $\boldsymbol{v}$ is any vector-valued function that satisfies the displacement boundary conditions

$$v_n=0, \text{ on } S^n, \tag{18}$$

and

$$v_t=0, \text{ on } S^t; \tag{19}$$

and the continuity condition

$$[\boldsymbol{v}] \equiv \boldsymbol{v}_+ - \boldsymbol{v}_- = 0, \quad \text{on } S^I, \tag{20}$$

on the material interface S^I, a weak discontinuity, with $[\boldsymbol{v}]$ the jump of $\boldsymbol{v}$ across S^I, $\boldsymbol{v}_+$ and $\boldsymbol{v}_-$ the values of $\boldsymbol{v}$ on the two sides of S^I. S^n in eq. (18) represents the displacement boundary segment that is smoothly supported in the normal direction; $v_n=\boldsymbol{n}\cdot\boldsymbol{v}$; $\boldsymbol{n}=(\cos\alpha, \sin\alpha)$ is the outer unit vector normal to S^n; and α is the angle between $\boldsymbol{n}$ and the positive x-axis. S^t in eq. (19) represents the displacement boundary segment that is fixed along the tangential of S^t; $v_t=\boldsymbol{t}\cdot\boldsymbol{v}$; $\boldsymbol{t}=(-\sin\alpha, \cos\alpha)$ is the unit vector tangential to S^t. S^t and S^n may coincide partially or completely.

$\boldsymbol{\varepsilon}$ in eq. (17) is the strain vector related to $\boldsymbol{v}$ by

$$\boldsymbol{\varepsilon} = L_d\boldsymbol{v}, \tag{21}$$

with L_d the differential operator

$$L_d = \begin{bmatrix} \dfrac{\partial}{\partial x} & 0 \\ 0 & \dfrac{\partial}{\partial y} \\ \dfrac{\partial}{\partial y} & \dfrac{\partial}{\partial x} \end{bmatrix}. \tag{22}$$

$\boldsymbol{\sigma}$ in eq. (15) is the stress vector related to $\boldsymbol{v}$ by the constitutive relation

$$\boldsymbol{\sigma} = \boldsymbol{D}\boldsymbol{\varepsilon}, \tag{23}$$

where $\boldsymbol{D}$ is the elastic matrix.

$\bar{\boldsymbol{p}}$ in eq. (17) represents the traction vector acting on the traction boundary S^σ. S^σ has no intersection with either

S^n or S^t. But S^n, S^n, and S^σ, compose the whole boundary of Ω, S, *i.e.*,

$$S = S^n \cup S^t \cup S^\sigma.$$

In NMM there are two reasons that prevent us from imposing the displacement boundary conditions as in FEM, where all the FE nodes match the problem domain. On the one hand, NMM allows the mathematical cover not to match the problem domain, implying that the displacement boundary condition cannot be satisfied in advance. On the other hand, in the presence of the material interface S^I, the NMM approximation $\boldsymbol{u}^h(\boldsymbol{r})$ may be discontinuous across S^I, because any mathematical patch, say M_i, cut through by S^I, is divided into two physical patches, say P_j and P_k, which have two independent approximations, $\boldsymbol{u}_j^h(\boldsymbol{r})$ and $\boldsymbol{u}_k^h(\boldsymbol{r})$. We do not need to get worried about these two issues. Zheng et al. [25] showed that matching nodes with the problem domain brings about little improvement of solution accuracy; instead the solution accuracy is determined by the mesh configuration for the local approximations.

In this study, the penalty method is selected to approximately enforce the displacement boundary condition and the interface continuity condition, leading to the functional fitted to NMM for the second order problem

$$\begin{aligned}\pi_n(\boldsymbol{v}) = \pi_c(\boldsymbol{v}) &+ \frac{1}{2}\int_{S^n} k_p v_n^2 \mathrm{d}S \\ &+ \frac{1}{2}\int_{S^t} k_p v_t^2 \mathrm{d}S + \frac{1}{2}\int_{S^I} k_p [\boldsymbol{v}]^2 \mathrm{d}S,\end{aligned} \tag{24}$$

where k_p is the user-defined penalty parameter.

As a result, while taking the first variation of π_n with regard to $\boldsymbol{v}$, we do not need to satisfy the displacement boundary conditions (18) and (19), and the continuity condition (20).

Of course, we can also utilize the Lagrange multiplier method to enforce the displacement boundary conditions and the interface continuity condition like refs. [13,25], which will result in an indefinite system of linear equations that need to be solved by specific techniques like ref. [33]. A solution to this issue is to introduce the augmented Lagrange multiplier method as in Ventura [34], only at the cost of several iterations for updating the multiplier.

3 Cover systems induced by a finite element mesh

In principle, an MC can be formed arbitrarily. According to the partition of unity theorem [32], the partition of unity subordinate to the MC always exists and all the weight functions can be made arbitrarily smooth. Up to now, however, in most applications and developments of NMM a finite element mesh has been chosen to construct MC because the weight functions associated with the finite element mesh are ready-made.

While deploying a finite element mesh, we do not have to match the mesh with Ω as long as it covers Ω, or equivalently, some elements in the mesh may have intersection with Ω. We call the mesh the mathematical mesh (MM).

Once MM is formed, a typical mathematical patch M_i consists of all the elements sharing node-i, called the star of node-i. Figure 6(a) displays the configuration of Ω and the triangular MM, where some stars are shadowed.

Theories and practices in the finite element analysis [30] tell us that the precision of the finite element analysis strongly depends on the mesh quality. So, in NMM a uniform MM is always favorite where all the elements takes on a standard shape, such as a square, an equilateral triangle or a right angled isosceles triangle. As a result, some nodes might be outside Ω as in Figure 6(a).

Cutting MM with the components of Ω, we obtain the physical patches and the physical mesh (PM), as shown in Figure 6(b), where the physical patches created from the node stars marked in Figure 6(a) are displayed. Each physical patch is associated with a node, and the node index is also the physical patch number. If a node star is cut by the crack into two distinct physical patches, a newly generated node is associated with one of the two physical patches, with the same coordinate as the original node. Figure 7 demonstrates this process. For this reason, in the physical mesh we still use the term "physical patch" instead of "star" because a physical patch might be misshapen due to cutting. Therefore, geometrically the node associated with a physical patch might be outside the physical patch. By intersecting the three neighboring physical patches, a manifold element shown in Figure 6(b) is just an ordinary element that might be partially cut off.

We make such a convention in specifying singular patches. Whenever a crack tip contacts an element, namely terminates inside the element or touches on an edge of the element, all the three physical patches covering the element are designated as singular patches.

Like a tent with a supporting center pole of unit height as shown in Figure 7(a), the weight function subordinate to a

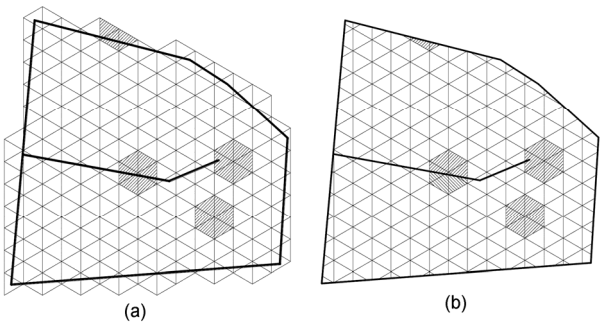

Figure 6 Finite element cover. (a) Mathematical mesh and some mathematical node stars (shadowed); (b) physical mesh and some physical patches (shadowed).

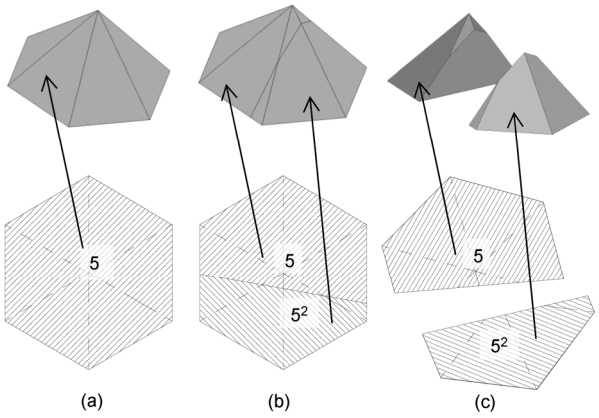

Figure 7 One node star is cut into two physical patches, each of them has its own weight function pointed by the arrows. (a) The star of node-5 in the mathematical mesh; (b) the lower physical patch has a newly generated node, indexed by 5^2, with the same coordinate as node 5 at this moment; (c) the two physical patches detach due to the ensuing movement.

star is formed by collecting the shape functions of all mathematical elements sharing node-*i*. If the star is cut into two physical patches by a crack, each physical patch has its own weight function, which will move with the physical patch, see Figure 7 for the demonstration.

4 NMM with multilayer finite element covers

We have pointed out that the inventor of NMM advocates a uniform mesh as MM so that the highest accuracy is reached. However, numerical problems often exhibit special features in small regions that require resolution and accuracy well beyond what is required in the rest of the domain. It is wasteful or prohibitively expensive to let local accuracy requirements dictate the global discretization and solution process. Therefore, since the invention of NMM, the inventor and many others have been considering how to implement structured local refinement. The goal of this section is to treat local demands in the framework of multilayer uniform meshes without overburdening the overall computation. Before our presentation, we make a brief review on the existing procedures for the structured local refinement.

4.1 Review on the structured local refinement

Whenever possible, according to the FEA theory [30], quadrilateral elements should be used in two dimensions, hexahedral elements in three dimensions, which, however, is almost impossible while handling complex geometries, unless irregular meshes as shown in Figure 1 are permitted, where nodes marked by ○ are hanging nodes. A hanging node is a vertex of a smaller element but hanging at an edge of the bigger element abutting on the smaller element.

In the setting of the finite difference methods, local refinement of uniform grids is easy because no compatibility between elements is involved, see ref. [35] for example.

In the setting of the finite element methods, to satisfy compatibility between elements, most finite element codes working with hanging nodes limit the maximum difference of refinement layers of adjacent elements to one (1-irregularity rule) (see, e.g., [36–40]). Figure 1 is an example of a 1-irregular mesh. Babuška and Miller [41] gave a posteriori error estimation yielded with 1-irregular mesh. In the literature, by k-irregularity rule (or k-layer hanging nodes) we mean this type of restriction where the maximum difference of refinement layers of adjacent elements is k. In this context, $k = 0$ corresponds to adaptivity with regular meshes and $k = \infty$ to adaptivity with arbitrary-layer hanging nodes.

The 1-irregularity rule brings stern restrictions to the mesh generation. For the 1-irregular mesh shown in Figure 8, for example, we hope to refine the shadowed triangle only, where singularity exists, obtaining the refinement shown in Figure 8(b). Because of the 1-irregularity rule, however, a further refinement of the neighboring elements as shown in Figure 8(c) is necessary even though such a refinement has little help to improve the resolution or the accuracy.

For the satisfaction of continuity on an interface between small and big element zones, there have been two commonly used techniques which essentially give rise to the same results. With the first technique, the hanging nodes have their own degrees of freedom and, the continuity on the interface is satisfied in a sense of the Lagrange multiplier method [42–45]. With the second technique, the hanging nodes are interpolated with vertex nodes [40]. Both techniques will cause the positive definiteness of the global stiffness matrix to be lost, necessitating complex hierarchical data structures that are hard to be amenable to NMM.

As an alternative, a super-element with variable number of edge nodes can be constructed. For example, Gupta [46] ever constructed a quadrilateral element each edge of which can have a middle node. So it can be used to implement 1-irregular local refinement [40]. But Gupta's technique cannot be used to construct elements with more than one edge node.

The quadrilateral element recently constructed by Cho and Im [47] and Baitsch and Hartmann [48] allows for arbitrary number of edge nodes, and in principle can be used to implement arbitrary-layer irregular local refinement. But

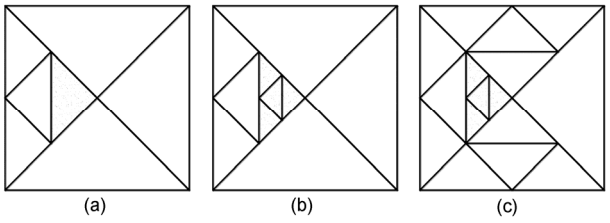

Figure 8 Trouble caused by 1-irregular rule. (a) Element marked for refinement; (b) refinement violating 1−irregularity rule; (c) additional refinements forced by 1−irregularity rule.

one must prepare sufficient element types in the finite element library, because the derivation of element shape functions has to be started from the scratch whenever a new node is added onto the edge. In addition, the numerical quadrature over a super-element with variable number of edge nodes becomes very complicated, necessitating further sub-division of the element and numerous integration points, because their shape functions are far more complicated than those of ordinary elements.

Up to now, all the structured local refinement techniques are performed on quadrilateral bilinear elements, excluding the use of more sophisticated element types.

All the limitations in the literature will be overcome in this study. To implement structured local refinement, we do not have to construct super-elements with variable number of edge nodes nor to introduce the Lagrange multiplier method.

4.2 NMM with multilayer finite element covers

In order to realize the best interpolation precision, we choose to implement structured local refinement in the setting of numerical manifold method, where each element takes on a standard shape, such as a square, an equilateral triangle or a right angled isosceles triangle.

Let's suppose that a given uniform mathematical mesh is called the first mathematical mesh layer, denoted by MM-1 subsequently. MM-1 covers the square domain Ω demonstrated in Figure 9(a), where Ω contains a crack represented by the dash dot line temporarily.

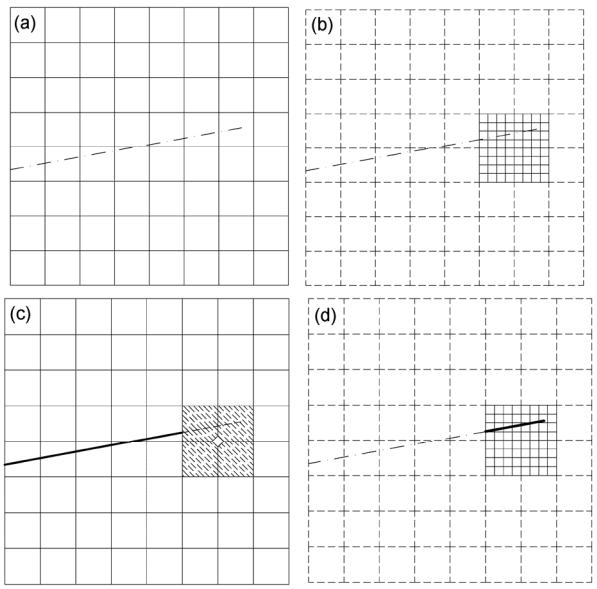

Figure 9 Generation of two physical mesh layers. (a) MM-1 covers the whole domain, with no info of the crack; (b) MM-2 is obtained by dividing some MM-1 elements around the crack tip. MM-2 has no info of the crack; (c) PM-1 is generated by cutting with the crack all the node stars in MM-1 except those covered by MM-2 which are marked by ◇. The elements not covered by MM-2 are called top elements of PM-1, which are not shadowed; (d) PM-2 is obtained by cutting MM-2 with the crack. All the PM-2 elements are top elements.

Now, around the crack tip we equally divide some elements in MM-1 into smaller elements. These smaller elements constitute the second mathematical mesh layer, MM-2, which merely covers the local domain around the crack tip, as shown in Figure 9(b).

We note that neither MM-1 nor MM-2 possesses any info of the crack.

By cutting with the crack all the MM-1 node stars except those covered by MM-2, we obtain the first physical mesh layer, PM-1, as shown in Figure 9(c). By cutting MM-2 with the crack, we obtain the second physical mesh layer, PM-2, as illustrated in Figure 9(d). We say PM-1 is below PM-2, as shown in Figure 10. Meanwhile, those PM-1 elements not covered by PM-2 are called top elements, which are the elements not shadowed as shown in Figure 9(c). Shortly, we will see that generating the physical meshes in this way can efficiently control the number of degrees of freedom.

If a point of interest, say $\boldsymbol{x}$, is contained in PM-1 only, the approximation at $\boldsymbol{x}$ takes on the form

$$\boldsymbol{u}(\boldsymbol{x}) = \boldsymbol{N}_e^1(\boldsymbol{x})\boldsymbol{d}_e^1, \tag{25}$$

where $\boldsymbol{N}_e^1$ represents the shape function matrix of PM-1 element Ω_e^1 that contains $\boldsymbol{x}$ and must be a top element; $\boldsymbol{d}_e^1$ is the vector of degrees of freedom of Ω_e^1.

If, however, $\boldsymbol{x}$ is contained in both elements Ω_e^1 of PM-1 and Ω_e^2 of PM-2, the solution at $\boldsymbol{x}$ is approximated by

$$\boldsymbol{u}(\boldsymbol{x}) = \boldsymbol{N}_e^1(\boldsymbol{x})\boldsymbol{d}_e^1 + \boldsymbol{N}_e^2(\boldsymbol{x})\boldsymbol{d}_e^2, \tag{26}$$

where $\boldsymbol{N}_e^i$ is the shape function matrix of element Ω_e^i

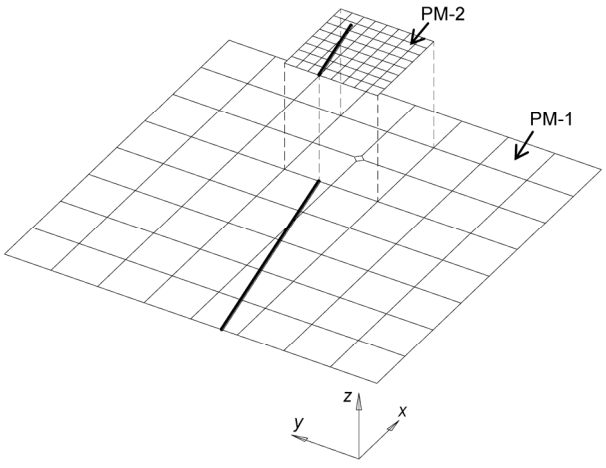

Figure 10 PM-1 is the global physical mesh. PM-2, around the crack tip, is finer than PM-1. PM-1 is below PC-2. All the PM-1 elements except those covered by PM-2 are top elements. All the PM-2 elements are top elements. All the top elements of PM-1 and PM-2 partition the whole problem domain exactly.

and $\boldsymbol{d}_e^i$ the vector of degrees of freedom of Ω_e^i, with superscript i = 1 or 2 denoting the mesh layer.

According to the way of generating the two physical meshes, eq. (26) has another implication: the first item $\boldsymbol{N}_e^1\boldsymbol{d}_e^1$ is always continuous because we do not cut the node stars of MM-1 covered by MM-2; the second item $\boldsymbol{N}_e^2\boldsymbol{d}_e^2$, determined by PM-2, reflects the characteristics of the solution around $\boldsymbol{x}$. In this way, the number of degrees of freedom is efficiently limited.

The above practice is actually equivalent to enriching the small region around the crack tip with the piecewise functions defined on PM-2 that is finer than PM-1 and is shown in Figure 9(d). Different from the conventional partition of unity methods, however, PM-2 has its own partition of unity, and the piecewise functions defined on PM-2 and constructed as in section 2.3.1 are not serving as the local approximations of those PM-1 physical patches around the crack tip. In this way, we can reach the maximum flexibility in local refinement. But this also leaves us with the issue of continuity across the PM-2 boundary.

By resorting to the approach of s-FEM [31], the continuity across the PM-2 boundary can be exactly satisfied by simply letting the PM-2 boundary nodes not participate in the interpolation, in other words, letting the degrees of freedom of these patches be zero. In this way, the displacements on the interface between PM-1 and PM-2 are determined by the displacements of nodes at PM-1's boundary, and the continuity is accordingly realized. In 1992, Fish [31] developed s-FEM, an excellent local refinement procedure that has been used extensively. However, s-FEM is not able to reflect the singularity or the discontinuity. Besides, s-FEM requires that local elements match the local domain and, it only involves two mesh layers. Sometimes, multilayer mesh refinement is necessary to be stated subsequently. In addition, to avoid the linear dependency of the system of equilibrium equations, s-FEM proposed that the local elements not align with the global mesh. Since the linear dependency due to alignment of the finer elements and the coarse elements is easy to solve by techniques such as the ε-disturbance method [4] or a more effective method [49], the alignment is persistent in this study so as to maintain the high precision. After all, the linear dependency issue disable those powerful solvers for the systems of linear equations. As a result, developing a local refinement scheme on the structurized meshes free from linear dependency is still a huge task, which is also one of the major topics the authors are studying.

To this point, the essential difference from the literature on the structured local refinement becomes clear. In the literature, only the local mesh, corresponding to PM-2, participates in the interpolation to the local domain, which causes the difficulty in the satisfaction of continuity on the interface between the fine mesh and the coarse mesh. In this study, however, the approximation at any point is constructed by all the mesh layers covering the point. It is clear that the displacement along the PM-2 boundary is determined by the displacement at the PM-1 nodes on the PM-1 boundary in alignment with the PM-2 boundary.

Sometimes we might need to further divide some MM-2 elements to constitute the third mathematical mesh, denoted by MM-3. Due to the generating way of the three mesh layers, only MM-1 is said to be the global mesh, both MM-2 and MM-3 are local meshes. As a result, the three mesh layers are hierarchical: MM-2 is above MM-1 but below MM-3.

Another purpose to deploy more than two mesh layers is to make the computational error distribution over the whole problem domain as even as possible, which is to be accomplished by the adaptive analysis.

Now we suppose that over Ω we have L mathematical mesh layers in all, MM-i, i= 1,⋯, L. Except the first layer MM-1 covering the whole domain, any higher layer, MM-i (i >1), is obtained by dividing some elements of its immediate predecessor MM-(i–1), and accordingly only covers local domains of Ω. As a result, all the L mathematical mesh layers have the relationship

$$\text{MM-1} \supset \text{MM-2} \supset \cdots \supset \text{MM-}(L-1) \supset \text{MM-}L,$$

and take on a hierarchical structure by the order that MM-1 is at the bottom, MM-2 is above MM-1 but below MM-3, and so on, until the top layer MM-L.

The same mathematical mesh layer may be composed of several separate element groups for covering separate local domains. Each element group may have a different element size. Figure 11 illustrates such a case, where MM-2 contains two separate element groups. The elements around the re-entrant angle on the left boundary are coarser than those around the crack tip, but both the element groups belong to MM-2.

Clearly, except the top layer MM-L, any MM-i (i<L) consists of two sets of elements: One set of elements are not covered by its immediate successor, MM-(i+1), and accordingly called top elements; another set of elements are covered by MM-(i+1). Figure 9(c) clearly demonstrates the two sets of elements in MM-1, where all those elements not

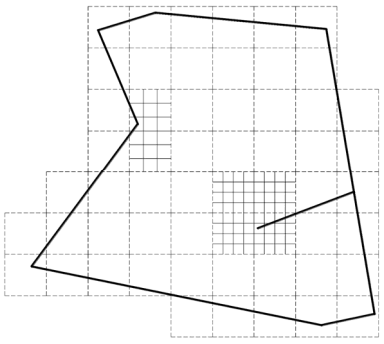

Figure 11 MM-2 contains two separate element groups: The elements around the re-entrant angle on the left and the elements around the crack tip. The two groups have different element size.

shadowed are top elements. By this definition, all the MM-*L* elements are top elements.

While generating the physical mesh PM-*i* corresponding to MM-*i*, we only cut with discontinuities the stars whose nodes are not coved by MM-(*i*+1) (see Figure 9(c) for explanation). In this way, the number of degrees of freedom can be controlled efficiently, because it is sufficient for the top layer to reflect the singularity and discontinuity.

With the *L* physical mesh layers, we approximate the solution at point $\boldsymbol{x}$ by

$$\boldsymbol{u}(\boldsymbol{x}) = \sum_{i=1}^{l} \boldsymbol{N}_e^i(\boldsymbol{x})\boldsymbol{d}_e^i, \tag{27}$$

where l is the number of mesh layers containing $\boldsymbol{x}$, suggesting that there are l elements containing $\boldsymbol{x}$, denoted by Ω_e^i, i=1,⋯, l. Ω_e^i belongs to PM-i. Ω_e^l is the top element of PM-i. Figure 12 demonstrates a case of two mesh layers containing $\boldsymbol{x}$. Associated with Ω_e^i are its shape function matrix $\boldsymbol{N}_e^i$ and degrees of freedom vector $\boldsymbol{d}_e^i$.

Again, the first l–1 items in eq. (27), $\boldsymbol{N}_e^i\boldsymbol{d}_e^i$, i=1,⋯, l–1, are continuous because the first l–1 mesh layers covering $\boldsymbol{x}$ do not participate in intersection with the discontinuities; the last item, $\boldsymbol{N}_e^l\boldsymbol{d}_e^l$, is discontinuous or singular, if the top element Ω_e^l has intersection with a discontinuity or singularity.

In order to assure the continuity of approximation (27) across the PM-i boundary (i>1), we assign zero to the degrees of freedom of all the PM-i boundary nodes. Therefore, the displacement on the PM-i boundary is determined by the displacement at PM-(i–1) nodes on the PM-(i–1) boundary in alignment with the PM-i boundary.

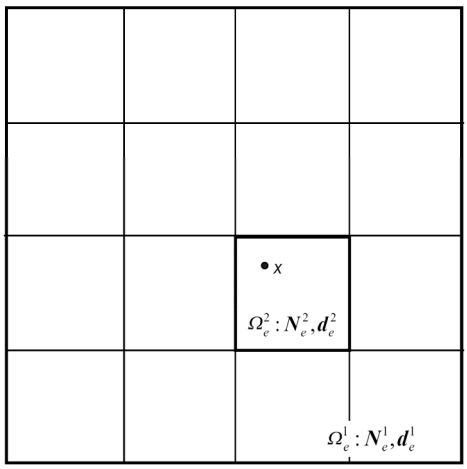

Figure 12 Point $\boldsymbol{x}$ is contained in two elements of two mesh layers. Marked by the inner thick lines, Ω_e^2 is the small element of PM-2. PM-1 element Ω_e^1 is the big element marked by the outer thick lines. Associated with Ω_e^i are its shape matrix $\boldsymbol{N}_e^i$ and degree of freedom vector $\boldsymbol{d}_e^i$.

Clearly, all the top elements from all the physical mesh layers exactly partition the problem domain Ω and hence serve as the basic units while integrating the weak form of the problem.

4.3 Formation of NMM system

A top element Ω_e^l of PM-l must be contained in the bigger elements Ω_e^j of lower layers PM-j, j = 1,⋯, l–1. According to approximation (27), all these l elements participate in the approximation over Ω_e^l. As a result, the stiffness matrix of Ω_e^l associated with functional π_n in eq. (24) involves the degrees of freedom of all these l elements, composed of l×l sub-matrices, typified by

$$\begin{aligned}\boldsymbol{K}_e^{ij} = &\int_{\Omega_e^l} \boldsymbol{B}_e^{i\mathrm{T}}\boldsymbol{D}\boldsymbol{B}_e^j \mathrm{d}\Omega + k_p\int_{S_l^n} \boldsymbol{N}_e^{i\mathrm{T}}\boldsymbol{C}\boldsymbol{N}_e^j \mathrm{d}S \\ &+ k_p\int_{S_l^t} \boldsymbol{N}_e^{i\mathrm{T}}\boldsymbol{S}\boldsymbol{N}_e^j \mathrm{d}S,\end{aligned} \tag{28}$$

with small dimensions independent of the number of mesh layers. For example, for a top element with no crack tip, both the row- and column-dimensions of $\boldsymbol{K}_e^{ij}$ are 16. Here, $\boldsymbol{N}_e^j$ represents the shape function matrix of Ω_e^j, j = 1,⋯, l. S_l^n and S_l^t are the edges of Ω_e^l, portions of the normal and tangential displacement boundaries S^n and S^t, respectively. $\boldsymbol{B}_e^i$ is defined by

$$\boldsymbol{B}_e^i = L_d\boldsymbol{N}_e^i. \tag{29}$$

Matrices $\boldsymbol{C}$ and $\boldsymbol{S}$ in eq. (28) are defined by

$$\boldsymbol{C} = \begin{bmatrix} c^2 & cs \\ cs & s^2 \end{bmatrix} \text{ and } \boldsymbol{S} = \begin{bmatrix} s^2 & -cs \\ -cs & c^2 \end{bmatrix}, \tag{30}$$

with c=cosα, s=sinα, and α inclination of the normal to S_l^n and S_l^t..

Similarly, the load vector of Ω_e^l consists of l sub-vectors, with a representative

$$\boldsymbol{q}_e^i = \int_{\Omega_e^l} \boldsymbol{N}_e^{i\mathrm{T}}\boldsymbol{b}\mathrm{d}\Omega + \int_{S_l^\sigma} \boldsymbol{N}_e^{i\mathrm{T}}\bar{\boldsymbol{p}}\mathrm{d}S, \tag{31}$$

where S_l^σ is the edge of Ω_e^l, portion of the traction boundary S^σ, on which traction $\bar{\boldsymbol{p}}$ loads.

Once sub-matrix $\boldsymbol{K}_e^{ij}$ given by eq. (28) and sub-vector $\boldsymbol{q}_e^i$ given by eq. (31) are formed, they are immediately assembled into the global stiffness matrix denoted by K, and the global load vector denoted by q, respectively. Since the dimensions of $\boldsymbol{K}_e^{ij}$ are very small and independent of the number of mesh layers, we are able to avoid the formation or storage of a very big top element stiffness matrix what-

ever number of mesh layers are deployed, which facilitates the creation of an even error distribution of the whole problem domain.

By solving the system $Kd = q$ for the vector of degrees of freedom d, we can retrieve any physical quantities of interest.

5 Numerical examples

In this section, we will demonstrate the capability of the proposed procedure with some examples with steep gradients or singularity. Except the last example, all examples are assumed to be in the plane stress state.

5.1 An infinite plate with a circular hole

Shown in Figure 13(a) is an infinite plate with a circular hole with radius $a = 1$ under the action of a horizontal stress $\sigma_\infty = 1$ at the infinite distance. The symmetry leads us to take a finite quadrant as the problem domain as illustrated in Figure 13(b), where the left and bottom boundaries are smoothly supported in the normal direction, the right and top boundaries are loaded by the traction specified by the analytical solution,

$$\sigma_x = \sigma_\infty \left[1 - \frac{a^2}{r^2}\left(\frac{3}{2}\cos 2\theta + \cos 4\theta\right) + \frac{3}{2}\frac{a^4}{r^4}\cos 4\theta\right], \quad (32.1)$$

$$\sigma_y = \sigma_\infty \left[-\frac{a^2}{r^2}\left(\frac{1}{2}\cos 2\theta - \cos 4\theta\right) - \frac{3}{2}\frac{a^4}{r^4}\cos 4\theta\right], \quad (32.2)$$

$$\tau_{xy} = \sigma_\infty \left[-\frac{a^2}{r^2}\left(\frac{1}{2}\sin 2\theta - \sin 4\theta\right) + \frac{3}{2}\frac{a^4}{r^4}\sin 4\theta\right], \quad (32.3)$$

with Young's modulus E= 1 and Poisson's ratio ν= 0.2.

Now we first design a uniform coarse mesh with an element size of 1.2 to cover the quadrant and obtain MM-1. Then, starting from the four MM-1 elements around the hole, we halve the elements in this region consecutively. Three halving operations yield MM-2 with a uniform element size of 1.2/8, as illustrated in Figure 14, which, by the nomenclature in the literature, is an 8-irregular mesh.

The stress distribution yielded by the three refinements is displayed in Figure 15, suggesting that with the mesh refinement, the calculated stress fast approximates the analytical solution.

By defining the relative energy error,

$$E_r = \frac{\int_\Omega \left(\boldsymbol{\varepsilon}^n - \boldsymbol{\varepsilon}^a\right)^{\mathrm{T}} \boldsymbol{D}\left(\boldsymbol{\varepsilon}^n - \boldsymbol{\varepsilon}^a\right) \mathrm{d}\Omega}{\int_\Omega \boldsymbol{\varepsilon}^{a\mathrm{T}} \boldsymbol{D}\boldsymbol{\varepsilon}^a \, \mathrm{d}\Omega}, \quad (33)$$

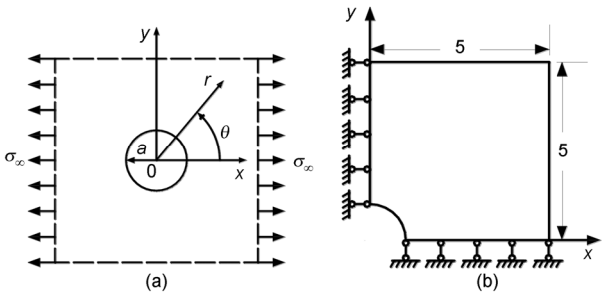

Figure 13 (a) Infinite plate with a hole; (b) computational model (example 5.1).

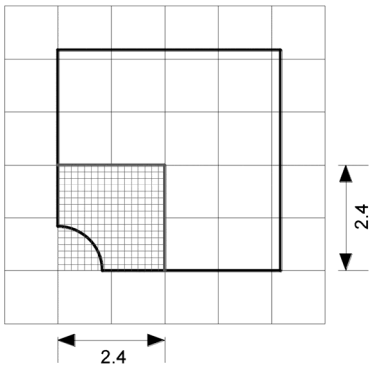

Figure 14 Two mesh layers (example 5.1).

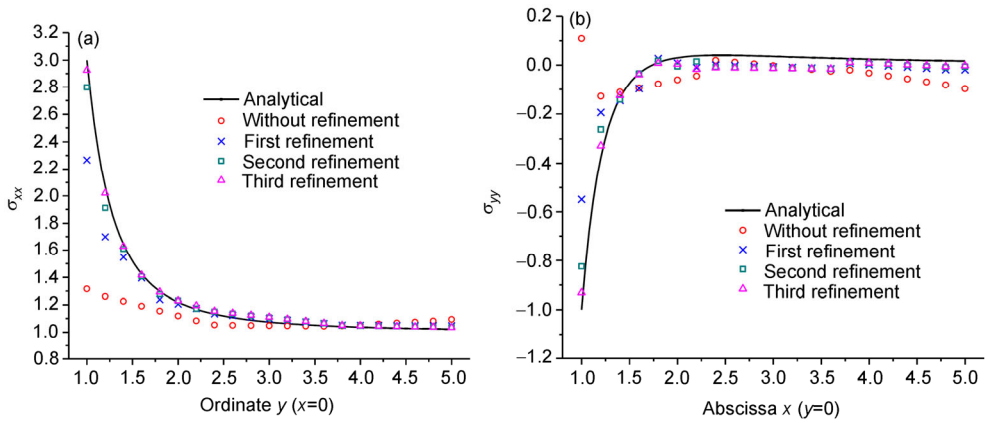

Figure 15 (Color online) Stress distribution yielded by three refinements (example 5.1). (a) σ_{xx} along axis y; (b) σ_{yy} along axis x.

we list the results in Table 2 with different refinements, indicating that the strain energy approaches from below the accurate value of 12.966.

This example and all the following examples appear to suggest such a fact that with mesh refinement the convergence rate of the strain energy or the stress intensity strength is not as fast as stresses or displacements at individual points.

5.2 A plate containing a horizontal crack

Now we consider a simple linear fracture problem. Shown in Figure 16 is a plate containing a horizontal crack with the parameters as follows: The uniform traction $\sigma = 1$, the plate length $L = 25$, the plate width $W = 10$, and the half crack length $a = 4$. The elastic parameters taken in the calculation are $E = 1$ and $\nu = 0.2$.

Three meshes are used as the global mesh with different element sizes 2.3, 1.8 and 1.6, respectively. Figure 17 displays the refined regions corresponding to three different global mesh size (GMS), in which the elements are to be halved twice. Figure 18 illustrates the mesh with a GMS of 2.3, a 4-irregular mesh.

The reference solution, given by Tada [50], is $K_{\mathrm{I}} = 3.9315$ and $K_{\mathrm{II}} = 0$. The calculated strength intensity factors are listed in Tables 3 to 5. From these results we can see that with refinement, the calculated solutions approach the reference solution.

Table 2 Relative errors (E_r) with refinement (example 5.1)

Halving times	Element size	Strain energy	E_r (%)	DOF
0	1.2	12.477	3.71	72
1	1.2/2	12.870	0.74	244
2	1.2/4	12.929	0.29	460
3	1.2/8	12.947	0.15	1016

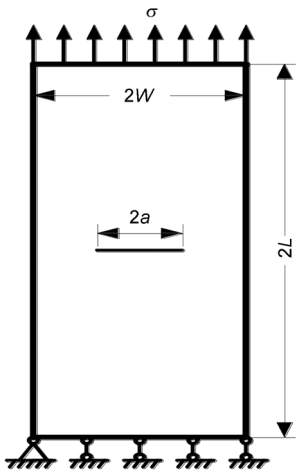

Figure 16 A plate loaded by a uniform tension (example 5.2).

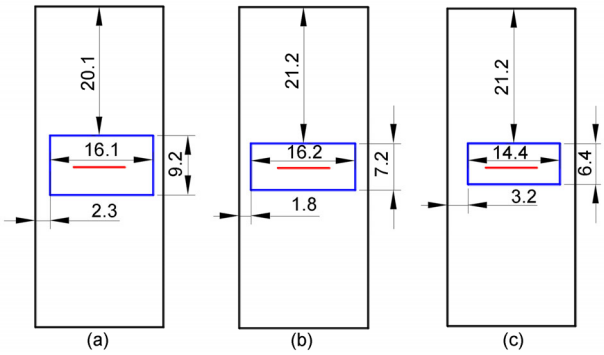

Figure 17 (Color online) Refined regions corresponding to three different global mesh sizes (GMS). (a) GMS=2.3; (b) GMS=1.8; (c) GMS=1.6 (example 5.2).

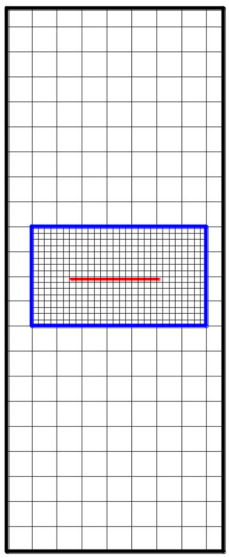

Figure 18 (Color online) A configuration of two mesh layers with GMS=2.3 (Example 5.2).

5.3 A plate containing a hole with two skew edge cracks

Shown in Figure 19(a) is a plate containing a hole with two skew edge cracks. The top surface of the plate is pulled by a uniformly distributed traction of σ=1, and the bottom surface is supported smoothly in the vertical direction. The plate dimensions include width W=10, length H=20, and the hole's radius r=2.5. The angle of the skew cracks, θ, varies between 0 and 60°. Two mesh layers are designed to cover the whole problem domain and the local region around the cracks, as shown in Figure 19(b). MM-1 has an element size of 2, and the MM-2 has an element size of 0.5.

Now let the crack have different length: a=0.7W, 0.6W, 0.5W, and 0.4W; and let θ=0°, 15°, 30°, 45°, and 60°.

The results are listed in Table 6, where F_1 and F_2 are defined by

$$F_1 = \frac{K_{\mathrm{I}}}{\sqrt{\pi a}} \quad \text{and} \quad F_2 = \frac{K_{\mathrm{II}}}{\sqrt{\pi a}};$$

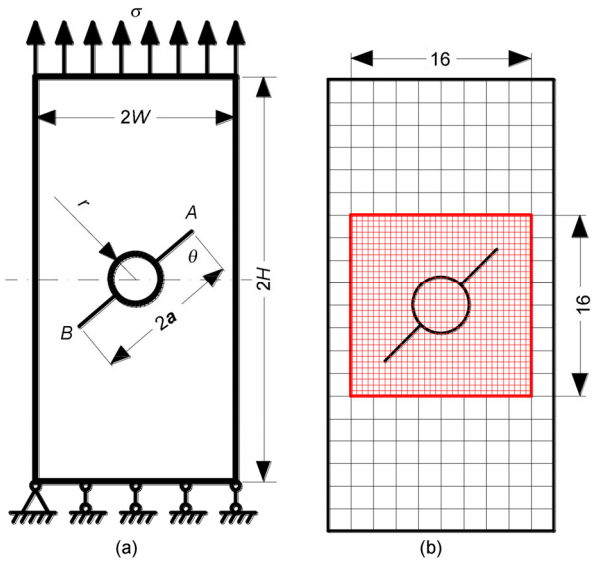

Figure 19 (Color online) (a) Dimensions and boundary conditions; (b) two mesh layers with the crack angle θ=45° (example 5.3).

Table 3 SIFs with GMS=2.3 (example 5.2)

Refinements	Left tip		Right tip		DOF
	K_{I}	K_{II}	K_{I}	K_{II}	
0	3.8554	0.0127	3.7609	0.0011	492
1	3.8927	0.0025	3.8829	0.0048	790
2	3.9029	0.0029	3.9036	0.0020	1984

Table 4 SIFs with GMS=1.8 (example 5.2)

Refinements	Left tip		Right tip		DOF
	K_{I}	K_{II}	K_{I}	K_{II}	
0	3.7635	0.0155	3.7807	0.0231	794
1	3.8984	0.0037	3.8829	0.0026	1212
2	3.9122	0.0009	3.9109	0.0024	2838

Table 5 SIFs with GMS=1.6 (Example 5.2)

Refinements	Left tip		Right tip		DOF
	K_{I}	K_{II}	K_{I}	K_{II}	
0	3.8787	0.0045	3.8784	0.0016	1000
1	3.9036	0.0052	3.9055	0.0048	1462
2	3.9130	0.0083	3.9134	0.0079	3196

and the rows marked by "R" give the reference solutions given by Chinese Aeronautical Establishment [51], suggesting that excellent agreements are reached.

5.4 A plate containing a long crack and a very short crack

Till now, all the PU-based methods are actually making such an implicit assumption that a crack cannot be so short that its two ends are both inside a patch, because no special solution is available to so short a crack. When encountering a very short crack, one has to make the mesh fine enough so that the two ends of the crack are not in the same patch. Here is an example.

Figure 20 illustrates a plate containing a long crack and a very short crack, with elastic parameters of E=1 and ν=0.2. An even upward traction, σ=1, is acting on the plate top. The plate bottom is smoothly supported in the vertical direction. All the dimensions are displayed in Figure 20.

Three mesh layers are used to cover the plate, the long crack and the short crack, respectively, as shown in Figure 21. Suppose that MM-1 has an element size of h_1. Let MM-2 have an element size of h_2=1/4h_1, and MM-3 have an element size of h_3=1/4h_2.

Table 7 lists the calculated results corresponding to different h_1, the element size of MM-1. For this example, we have no analytical solution or reference solution available. By scrutinizing the results, however, K_{I} is nearly propor-

Table 6 Results with different crack lengths and angles (example 5.3)

θ	Tip	0.7		0.6		0.5		0.4	
		F_1	F_2	F_1	F_2	F_1	F_2	F_1	F_2
	A	1.549	-0.001	1.379	-0.001	1.273	0.000	1.207	0.000
0	B	1.549	0.001	1.379	0.001	1.274	0.001	1.207	0.001
	R*)	1.574	0.000	1.396	0.000	1.286	0.000	1.216	0. 000
	A	1.446	0.270	1.290	0.258	1.191	0.236	1.120	0.194
15	B	1.446	0.271	1.289	0.259	1.189	0.237	1.120	0.195
	R	1.462	0.291	1.303	0.263	0.198	0.237	1.126	0.192
	A	1.142	0.491	1.028	0.457	0.944	0.416	0.870	0.338
30	B	1.140	0.491	1.026	0.457	0.944	0.416	0.869	0.337
	R	1.155	0.504	1.038	0.463	0.948	0.417	0.872	0.336
	A	0.723	0.581	0.652	0.539	0.583	0.485	0.514	0.390
45	B	0.721	0.578	0.652	0.539	0.583	0.484	0.513	0.390
	R	0.731	0.584	0.654	0.541	0.585	0.486	0.512	0.388
	A	0.297	0.494	0.258	0.463	0.213	0.418	0.151	0.335
60	B	0.297	0.491	0.258	0.460	0.213	0.416	0.151	0.333
	R	0.300	0. 500	0.257	0. 465	0.210	0.418	0.147	0.332

*) "R" represents Reference Solution [49].

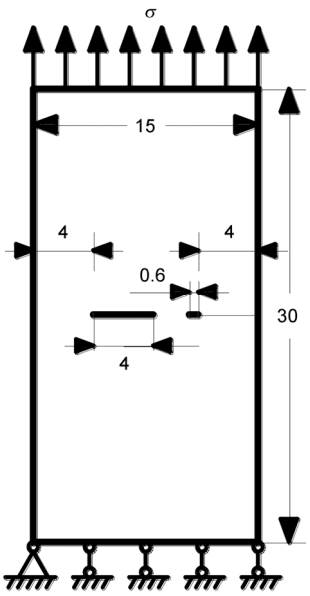

Figure 20 A plate containing a long crack and a very short crack (example 5.4).

Table 7 Calculated SIFs (example 5.4)

GMS	Long crack				Short crack			
	Left end		Right end		Left end		Right end	
	K_{I}	K_{II}	K_{I}	K_{II}	K_{I}	K_{II}	K_{I}	K_{II}
2.4	2.6268	0.0073	2.6127	0.0106	1.1091	0.0010	1.0352	0.0008
2.0	2.6359	0.0002	2.6139	0.0000	1.1137	0.0001	1.0876	0.0001
1.6	2.6574	0.0006	2.6291	0.0005	1.1053	0.0001	1.0893	0.0001

tional to the square root of the crack length, in agreement with our knowledge from linear facture mechanics.

5.5 A semi-infinite elastic body under the action of a concentrated force

Lastly, we consider a semi-infinite elastic body under the action of a downward concentrated force, which is the strongest singularity that is acceptable to elasticity theory. Under the coordinate system shown in Figure 22(a), we have the analytical solution as follows:

$$\sigma_x = -\frac{2F}{\pi}\frac{x^3}{\rho^4}, \tag{34.1}$$

$$\sigma_y = -\frac{2F}{\pi}\frac{xy^2}{\rho^4}, \tag{34.2}$$

$$\sigma_{xy} = -\frac{2F}{\pi}\frac{x^2y}{\rho^4}, \tag{34.3}$$

$$u_\rho = -\frac{2F}{\pi E}\cos\phi\ln\rho - \frac{(1-v)F}{\pi E}\phi\sin\phi + I\cos\phi, \tag{35.1}$$

$$u_\phi = \frac{2F}{\pi E}\sin\phi\ln\rho - \frac{(1-v)F}{\pi E}\phi\cos\phi + \frac{(1+v)F}{\pi E}\sin\phi - I\sin\phi. \tag{36.2}$$

Since the example is strongly singular, four mesh layers are designed as shown in Figure 22(b), with element sizes of 1.0, 0.5, 0.25 and 0.125, respectively. The left and the bottom boundaries are loaded with the traction calculated by equations (34.1) to (34.3). The right boundary is smoothly supported in the horizontal direction due to the symmetry. In order to remove the rigid body displacement mode, the vertical displacement at the bottom right corner of the model is imposed by the exact value determined by equation (35.1) with $F = 1$, $I = 10$, ρ=10 and φ=0.

In order to compare the proposed procedure with the existing methods in the literature, we specify the coarse elements abutting on the finer meshes as Gupta's transition element [46]. Such an element can have 0–4 edge nodes and can be used to construct a 1-irregular mesh through matching one Gupta's element with two small elements side-by-side.

All the elements are specified as ordinary rectangular elements with no special solutions introduced.

Figure 23 displays the vertical displacements along axis y (φ=90°) and the line of φ=45°.

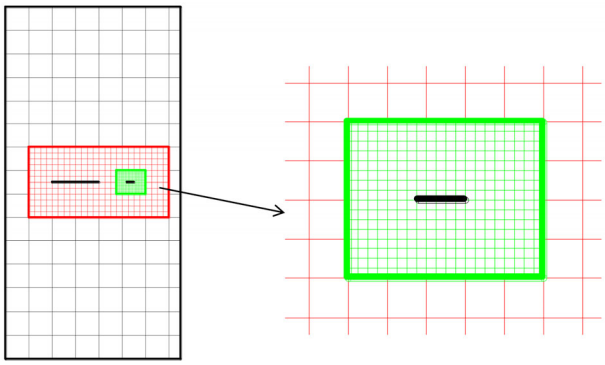

Figure 21 (Color online) Three mesh layers with GMS=2 (example 5.4).

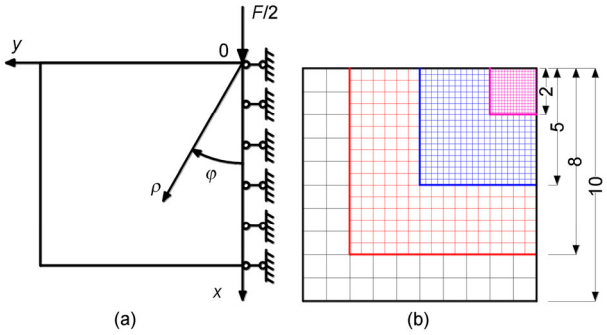

Figure 22 (Color online) (a) A semi-infinite elastic body under the action of a concentrated force; (b) four mesh layers (example 5.5).

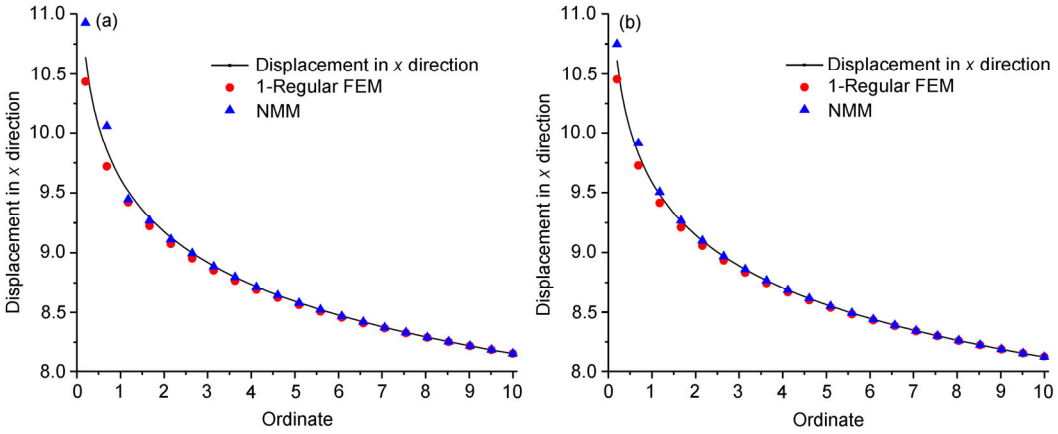

Figure 23 (Color online) (a) Vertical displacement along axis y (example 5.5); (b) vertical displacement along the line of ϕ=45° (example 5.5).

The proposed procedure reaches higher accuracy than the transition element method, suggesting that hanging nodes are not helpful to accuracy because their values are determined by the vertex nodes.

6 Discussion and conclusions

By introducing multilayer covers that cover different local domains with different element sizes, we realize the local refinement on the structured uniform meshes. When the exact solution does not have a recognizable structure, as in highly heterogeneous media, then h-extensions with uniform mesh refinement should be utilized so that the highest accuracy and convergence are reached.

We never form or save any top element matrices, which might have very big dimensions in case of the presence of multilayer covers. Instead, we directly assemble into the global matrices the sub-matrices of top element matrices whose dimensions are small and independent of cover layers. In this way, there is no limitation to the number of cover layers, facilitating the creation of an even error distribution over the whole problem domain.

By extrapolation of the finite element method, what's more, we can derive a very accurate solution from two consecutively refined meshes that must be structured [52]. This and adaptive refinement with uniform meshes will be our next research subjects.

Yet, we must admit that the proposed procedure does not overcome linear dependency, although there have been robust solvers to solve the systems of linear equations of linear dependency. To utilize those high efficient solutions for the systems of linear equations, it is necessary to develop local refinement methods based on the structurized meshes but free from linear dependency, and this is just one of the topics we are conducting.

This work was supported by the National Basic Research Program of China ("973" Project) (Grant Nos. 2011CB013505 & 2014CB047100), and the National Natural Science Foundation of China (Grant Nos. 11572009 & 51538001).

1 Shi G H. Manifold method of material analysis. In: Transactions of the 9th Army Conference on Applied Mathematics and Computing. Report No. 92–1, U.S. Army Research Office, Minneapolis, MN, 1991. 57–76
2 Lin J S. A mesh-based partition of unity method for discontinuity modeling. Comput Method Appl M, 2003, 192: 1515–1532
3 Babuška I, Melenk J M. The partition of unity method. Int J Numer Meth Eng, 1997, 40: 727–758
4 Strouboulis T, Copps K, Babuška I. The generalized finite element method. Comput Method Appl M, 2001, 190: 4801–4191
5 Dolbow J, Moës N, Belytschko T. An extended finite element method for modeling crack growth with frictional contact. Comput Method Appl M, 2001, 190: 6825–6846
6 Belytschko T, Lu Y Y, Gu L. Element–free galerkin methods. Int J Numer Meth Eng, 1994, 37: 229–256
7 Terada K, Asai M, Yamagishi M. Finite cover method for linear and non–linear analyses of heterogeneous solids. Int J Numer Meth Eng, 2003, 58: 1321–1346
8 Chen G Q, Ohnishi Y, Ito T. Development of high–order manifold method. Int J Numer Meth Eng, 1998, 43: 685–712
9 Jiang Q H, Zhou C B, Li D Q. A three–dimensional numerical manifold method based on tetrahedral meshes. Comput Struct, 2009, 87: 880–889
10 Tian R, Yagawa G, Terasaka H. Linear dependence problems of partition of unity-based generalized FEMs. Comput Method Appl M, 2006, 195: 4768–4782
11 An X M, Li L X, Ma G W, et al. Prediction of rank deficiency in partition of unity–based methods with plane triangular or quadrilateral meshes. Comput Method Appl M, 2011, 200: 665–674
12 An X M, Liu X Y, Zhao Z Y, et al. Proof of linear independence of flat-top PU-based high-order approximation. Eng Anal Bound Elem, 2014, 44: 104–111
13 Cai Y C, Zhuang X Y, Augarde C. A new partition of unity finite element free from the linear dependence problem and possessing the delta property. Comput Method Appl M, 2010, 199: 1063–1043
14 Terada K, Kurumatani M. Performance assessment of generalized elements in the finite cover method. Finite Elem Anal Des, 2004, 41: 111–132
15 Zheng H, Xu D D. New strategies for some issues of numerical manifold method in simulation of crack propagation. Int J Numer Meth Eng, 2014, 97: 986–1010
16 Wu Z J, Wong L N Y. Frictional crack initiation and propagation analysis using the numerical manifold method. Comput Geotech, 2012, 39: 38–53

17 Kurumatani M, Terada K. Finite cover method with multi–cover layers for the analysis of evolving discontinuities in heterogeneous media. Int J Numer Meth Eng, 2009, 79: 1–24
18 Ma G W, An X M, Zhang H H, et al. Modeling complex crack problems using the numerical manifold method. Int J Fracture, 2009, 156: 21–35
19 An X M, Fu G Y, Ma G W. A comparison between the NMM and the XFEM in discontinuity modeling. Int J Comput Methods, 2012, 9: 1240030
20 Ning Y J, An X M, Ma G W. Footwall slope stability analysis with the numerical manifold method. Int J Rock Mech Min, 2011, 48: 964–975
21 Wu Z J, Wong L N Y. Frictional crack initiation and propagation analysis using the numerical manifold method. Comput Geotech, 2012, 39: 38–53
22 Zhang Z N, Zheng H, Ge X R. Triangular element partition method with consideration of crack tip. Sci China Tech Sci, 2013, 56: 2081–2088
23 Zhang Z R, Zhang X W, Yan J H. Manifold method coupled velocity and pressure for Navier–Stokes equations and direct numerical solution of unsteady incompressible viscous flow. Comput Fluids, 2010, 39: 1353–1365
24 Fan H, Zheng H. MRT-LBM-based numerical simulation of seepage flow through fractal fracture networks. Sci China Tech Sci, 2013, 56: 3115–3122
25 Zheng H, Liu Z J, Ge X R. Numerical manifold space of Hermitian form and application to Kirchhoff's thin plate problems. Int J Numer Meth Eng, 2013, 95: 721–739
26 Li S C, Li S C, Cheng Y M. Enriched meshless manifold method for two- dimensional crack modeling. Theor Appl Fract Mec, 2005, 44: 234–248
27 Zheng H, Liu F, Li C G. Primal mixed solution to unconfined seepage flow in porous media with numerical manifold method. Appl Math Model, 2015, 39: 794–808
28 Zheng H, Liu F, Li C G. The MLS-based numerical manifold method with applications to crack analysis. Int J Fracture, 2014, 190: 47–166
29 Zhang H H, Zhang S Q. Extract of stress intensity factors on honeycomb elements by the numerical manifold method. Finite Elem Anal Des, 2012, 59: 55–65
30 Szabó B, Babuška I. Introduction to Finite Element Analysis: Formulation, Verification and Validation. Wiley: Chichester, 2011
31 Fish J. The s-version of the finite element method. Comput Struct, 1992, 43: 539–547
32 Spivak M. Calculus on Manifolds. Benjamin, New York, 1965
33 Zheng H, Li J L. A practical solution for KKT systems. Numer Algorithms, 2007, 46: 105–119
Ventura G. An augmented Lagrangian approach to essential boundary conditions in meshless methods. Int J Numer Meth Eng, 2002, 53: 25–842
34 Durbin P A, Iaccarino G. An approach to local refinement of structured grids. J Comput Phys, 2002, 181: 639–653
35 Paszynski M, Kurtz J, Demkowicz L. Parallel, fully automatic hp–adaptive 2D finite element package, TICAM Report 04–07. The University of Texas at Austin, 2004
36 Peano A G. Hierarchies of conforming finite elements for plane elasticity and plate bending. Comput Math Appl, 1976, 2: 211–224
37 Rachowicz W, Demkowicz L. An hp–adaptive finite element method for electromagnetics, Part II, a 3D implementation. Int J Numer Meth Eng, 2002, 53: 147–180
38 Tian L, Chen F, Du Q. Adaptive finite element methods for elliptic equations over hierarchical T–meshes. J Comput Appl Math, 2011, 236: 878–891
39 Fries T P, Byfut A, Alizada A, et al. Hanging nodes and XFEM. Int J Numer Meth Eng, 2011, 86: 404–430
40 Babuška I, Miller A. A feedback finite element method with a posteriori error estimation: Part I, the finite element method and some basic properties of the a posteriori error estimator. Comput Method Appl M, 1987, 61: 1–40
41 Belgacem F B. The mortar finite–element method with Lagrange multipliers. Numer Math, 1999, 84: 173–197
42 McDevitt T W, Laursen T A. A mortar–finite element formulation for friction contact problems. Int J Numer Meth Eng, 2000, 48: 1525–1547
43 Wheeler M F, Yotov I. Multigrid on the interface for mortar mixed finite–element methods for elliptic problems. Comput Method Appl M, 2000, 184: 287–302
44 Casadei F, Rimoli J J, Ruzzene M. A geometric multiscale finite element method for the dynamic analysis of heterogeneous solids. Comput Method Appl M, 2013, 263: 56–70
45 Gupta A K. A finite element for transition from a fine to a coarse grid. Int J Numer Meth Eng, 1978, 12: 35–45
46 Cho Y S, Im S. MLS-based variable-node elements compatible with quadratic interpolation, Part I, formulation and application for non-matching meshes. Int J Numer Meth Eng, 2006, 65: 494–516
47 Baitsch M, Hartmann D. Piecewise polynomial shape functions for hp–finite element methods. Comput Method Appl M, 2009, 198: 1126–1137
48 Zheng H, Yang Y T. A direct solution to linear dependency issue arising from GFEM. In: Computer Methods and Recent Advances in Geomechanics-Proceedings of the 14th Int. Conference of International Association for Computer Methods and Recent Advances in Geomechanics, IACMAG, Paper No. 1092165, Keoto, Japan, 2014
49 Tada H, Paris P C, Irwin G R. The Stress Analysis of Cracks Handbook. New York: ASME Press, 2000
50 Establishment C A. Handbook of the Stress Intensity Factor (in Chinese). Beijing: Science Press, 1993
51 Blum H, Lin Q, Rannacher R. Asymptotic error expansion and Richardson extrapolation for linear finite elements. Numer Math, 1986, 49: 11–37